



## **Dynamics of Contaminant Flow Through Porous Media Containing Random Adsorbers**

Downloaded from: <https://research.chalmers.se>, 2025-03-09 14:19 UTC

Citation for the original published paper (version of record):

Pettersson, K., Sasic Kalagasidis, A., Modin, O. et al (2025). Dynamics of Contaminant Flow Through Porous Media Containing Random Adsorbers. *Transport in Porous Media*, 152.  
<http://dx.doi.org/10.1007/s11242-025-02150-y>

N.B. When citing this work, cite the original published paper.

# Dynamics of contaminant flow through porous media containing random adsorbers

Kaj Pettersson<sup>1\*</sup>, Albin Nordlander<sup>2</sup>, Angela Sasic Kalagasidis<sup>2</sup>,  
Oskar Modin<sup>2</sup>, Dario Maggiolo<sup>1</sup>

<sup>1</sup>\*Department of Mechanics & Maritime Sciences, Chalmers University  
of Technology, Chalmersplatsen 4, Göteborg, 412 96, Sweden.

<sup>2</sup>Department of Architecture & Civil Engineering, Chalmers University  
of Technology, Chalmersplatsen 4, Göteborg, 412 96, Sweden.

\*Corresponding author(s). E-mail(s): [kajp@chalmers.se](mailto:kajp@chalmers.se);  
Contributing authors: [Angela.Sasic@chalmers.se](mailto:Angela.Sasic@chalmers.se);  
[oskar.modin@chalmers.se](mailto:oskar.modin@chalmers.se); [maggiolo@chalmers.se](mailto:maggiolo@chalmers.se);

## Abstract

Many porous media are mixtures of inert and reactive materials, manifesting spatio-chemical heterogeneity. We study the evolution of scalar transport in a chemically heterogeneous material that mimics a green roof soil substrate, fractionally composed of inert and reactive adsorbing particles. These adsorbing particles are equivalent to biochar within a real soil substrate. The scalar transport evolution is determined using experiments and simulations calibrated from experimental data. Experiment 1 is used to determine the equilibrium capacity and adsorption rate of two biochar types when immersed in a methylene blue solution. Breakthrough curves of a packed bed of glass beads with randomly interspersed biochar are determined in experiment 2. Simulations are then run to investigate the solute transport and adsorption dynamics at the pore-scale. An analytical model is proposed to capture the behavior of the biochar adsorption capacity and the simulation results are compared with experiment 2. A pore-scale analysis showed that uniformly sized beds are superior in contaminant breakthrough reduction, which is related to the adsorptive surface area and the rate at which adsorption capacity is reached. Cases using the adsorption capacity model display a tight distribution of particle surface concentration at later simulation times, indicating maximum possible adsorption. The beds with dissimilar

particle sizes create more channeling effects which reduce adsorptive particle efficiency and consequently higher breakthrough concentration profiles. Comparison between experiments and simulations show good agreement. Improved biochar performance can be achieved by maintaining particle size uniformity alongside high adsorption capacity and adsorption rates appropriate to the rainfall intensity.

**Keywords:** biochar, lattice Boltzmann, experiment, adsorption, methylene blue

## Article Highlights

- Experiments on biochar adsorption of methylene blue compared to simulations, with good agreement.
- Simple analytical model proposed to capture biochar adsorption capacity, results compared to experiments.
- Performance inferior in polydisperse beds due to underutilized particles and inhomogeneous concentration front profile.

## 1 Introduction

Porous media containing a proportion of inert and chemically reactive elements can be found in biology in the form of biofilters, bioreactors, and organic tissue. They are also found in geological elements such as rocks or soils, which are also highly chemically heterogeneous, containing a wide variety of chemically dissimilar minerals and/or organic elements. Research into this type of porous media has formerly been primarily driven by the petrochemical industry, however this has shifted in recent years to a more environmental focus. Green roofs are one such example, consisting of living greenery ranging from trees to grasses growing in a soil substrate whose composition can vary widely, from crushed brick to manure to peat moss. The benefits of green roofs in urban environments are well documented, such as their contributions to the reduction in urban noise, air, and water pollution; their effects on the urban heat island

57 as well as building envelopes themselves; and urban rainwater runoff management  
58 [Aguilar Fajardo et al. \(2022\)](#).

59 Green roofs require regular maintenance, including the administration of fertilizer  
60 upon installation and potentially thereafter as the need arises. The fertilizer consists  
61 of a fast-acting agent which gives the plants a boost to survive the initial period of  
62 installation and establish themselves; and longer-acting nutrients which aim to keep  
63 the additional required maintenance to a minimum. Excess fertilizer which cannot be  
64 stored by the soil or used directly by the vegetation can be carried by rainwater from  
65 the soil through the drainage system to locations where it acts as a contaminant [Wang  
66 et al. \(2017\)](#). The addition of biochar to the soil to adsorb excess fertilizer (contaminant  
67 or solute) is currently being put forth as viable solution to this problem.

## 68 **1.1 Biochar in green roofs**

69 Biochar is essentially any organic material that has been carbonized under high tem-  
70 perature through a process known as pyrolysis and can vary in material properties  
71 and morphology significantly. A thorough overview of the types of biochar in use  
72 commercially can be found in [Novotný et al. \(2023\)](#).

73 Biochar is incorporated into green roof soil via three strategies; random application  
74 to the top of the bedding material, thorough mixing into the substrate composition  
75 prior to vegetation, and set as a layer at the bottom of the substrate. Thorough  
76 mixing and layering at the soil base are considered the most effective, with the latter  
77 shown to be effective for reducing the leaching of total nitrogen and total phosphorous  
78 [Kuoppamäki et al. \(2016\)](#). The proportion of applied biochar varies, from 5% by  
79 weight/volume up to about 40%, however excessive proportions of biochar will have  
80 adverse effects on plant growth and contribute to increased contamination [Xiang et al.  
81 \(2021\)](#).

82 There are few large-scale projects incorporating biochar use on green roofs though a  
83 few exist, such as the NWE CASCADE project, in which France intends to implement  
84 the use of biochar to enhance stormwater management within the Brittany region.  
85 Other similar solutions will likely be implemented within a larger initiative led by  
86 Bloomberg Philanthropies as touched upon in [Senadheera et al. \(2024\)](#).

87 The industrial-scale implementation is dependent upon several factors, such as the  
88 ecological impact of large-scale biochar use and the release of additional contaminants  
89 present within or on the surface of biochar as a result of its preparation and function.  
90 For example, [Premarathna et al. \(2023\)](#) discusses the almost complete removal of  
91 ammonia from the soil when excessive biochar is applied, which can be problematic  
92 for soil health. Another key factor is availability of biochar itself, given the different  
93 feedstock and treatment methods for its creation. A final major consideration is the  
94 lifetime of the biochar as an adsorbent and its end-of-life handling. Little work has been  
95 done on the effects of aging on biochar performance due to limited long-term projects  
96 but what is known is that degrading performance is dependent upon the contaminant  
97 and environmental conditions. For example, if the primary goal of the biochar is to  
98 trap micro and nano-plastics (MPs and NPs) then both the aging of the biochar *and*  
99 the plastics themselves play an important role in the removal efficiency [Ji et al. \(2024\)](#).  
100 Physical degradation of the biochar also occurs during the aging process and leads  
101 to biochar dust, which no longer serves its purpose of entrapping pollutants but can  
102 act to spread captured plastics or heavy metals due to its increased mobility. It has  
103 been shown the granulated biochar in particular is more resistant to this degradation  
104 process, thus making it more suitable for applications such as green roofs where the  
105 environmental exposure is high [Lee and Kwon \(2024\)](#).

106 Related to the issue of biochar disposal is the issue of regeneration, which heavily  
107 depends upon the captured contaminants. It is possible to regenerate biochar that  
108 has captured MPs/NPs using organic solvents such as acetone, however this is not

feasible in a green roof environment due to environmental concerns. Water rinsing performs relatively poorly for removing carbon-based adsorbents but can be used [Ji et al. \(2024\)](#). Adsorbed copper can be almost completely recovered [Bashir et al. \(2023\)](#), as can cadmium [Cui et al. \(2022\)](#). Biochar regeneration over five adsorption-desorption cycles was assessed with regard to volatile organic compounds (VOCs) with reported 88% to 96% regeneration [Rajabi et al. \(2021\)](#). While these reports are promising, the scalability for some of the processes used for regeneration is in doubt as they are either inappropriate for green roofs due to their open nature, or less efficient if alternatives are used [Gupta et al. \(2020\)](#).

Biochar may raise the production costs of green roofs, resulting in higher final prices for these products [Khan et al. \(2021\)](#). To evaluate its profitability for both producers and end users, it is essential to compare its effects against using fertilizers alone or in combination with fertilizers [Ye et al. \(2020\)](#). Additionally, given its environmental benefits—such as minimizing nutrient leakage and boosting carbon sequestration—efforts are underway to improve cost calculation models to include both private and societal costs and benefits [Campion et al. \(2023\)](#). However, these calculations are highly case-specific, influenced by factors like location, feedstock, scale, pyrolysis conditions, biochar pricing, and crop type. To promote greater adoption of biochar, [Campion et al. \(2023\)](#) suggest developing standardized calculation models and emphasizing additional societal benefits of biochar, such as improved water retention. While the proposed model is comprehensive, it remains unclear how potential hazards associated with biochar [Xiang et al. \(2021\)](#) will be addressed with it. Thus, the technoeconomic benefits of biochar will be a focus of future research.

## 1.2 Biochar adsorption capabilities

Many variants of biochar have been employed for the purpose of removing contaminants in a soil or packed bed. [Afroze et al. \(2016\)](#) determined the adsorption of

135 methylene blue (MB) by eucalyptus bark biomass in a packed bed and found that it  
 136 performs well in the removal of dye-containing effluents. [Dawood et al. \(2019\)](#) ana-  
 137 lyzed the adsorption of MB in pine cone biochar in a packed bed column of Kaolin  
 138 clay and utilized several analytical models to determine breakthrough curves. These  
 139 curves were compared under varying experimental conditions and the biochar/clay  
 140 packed bed was found to perform best under low flow rates, high MB concentration,  
 141 and larger bed depth. [Zanin Lima et al. \(2023\)](#) analyzed competitive sorption and des-  
 142 orption of zinc, cadmium, and lead between compost, biochar, and peat. They found  
 143 that biochar had the highest adsorption capacity and lowest desorption rate, with lead  
 144 removal being the most effective. [Beesley et al. \(2010\)](#) examined the efficacy of biochar  
 145 and greenwaste compost on the reduction of zinc, cadmium, and copper within soils  
 146 and found them to be beneficial in the control of pollutants. [Pita et al. \(2024\)](#) provided  
 147 a review of the work associated with the use of biomass on the removal of pharma-  
 148 ceutical compounds and reported that biochar made from a variety of plants; such as  
 149 rice husks, corn, sawdust, and sugar cane, was the most effective in many industrial  
 150 applications, partly due to their high adsorption capacity. While the aforementioned  
 151 studies are valuable in understanding biochar as an adsorbent for a variety of contam-  
 152 inants, we are unable to identify the mechanisms by which it performs best, such as  
 153 available adsorbing surface area, effect on the flow field, or their pore storage capac-  
 154 ity. For this level of detail we must utilize numerical models which can describe such  
 155 systems and provide the level of detail we require.

156 The physical process of contaminant adsorption in a flow field is described mathe-  
 157 matically by the advection-diffusion of species, combined with adsorption/desorption;  
 158 a model which is present across many fields of application. This general model is used  
 159 to describe processes such as post-combustion CO<sub>2</sub> capture [Pröll et al. \(2016\)](#), deter-  
 160 mining optimal geometry of granular heat exchangers [Mitra et al. \(2018\)](#), analyzing  
 161 methane adsorption in subsurface shale deposits [Li et al. \(2016\)](#), and describing the

behavior of photocatalytic textiles [Robin et al. \(2016\)](#) to name a few. Investigations into the dominant factors affecting adsorption rates and capacity have shown that particle and pore morphology play an important role [Liapis et al. \(1999\)](#); [Jareteg et al. \(2022\)](#). Adsorption rates themselves also strongly determine the process evolution [Marin et al. \(2014\)](#), with lower rates determining adsorption quantity by reaction duration, and higher rates controlling quantity through reaction rate [Zakirov et al. \(2023\)](#). Non-isothermal systems can result in high heterogeneity of concentration and temperature, with performance suffering from regions of stagnant flow and increased near-wall breakthrough [Verma and Mewes \(2009\)](#).

When one considers a transported reactive species adsorbed locally by reactive elements within a porous matrix; understanding the underlying interactions which determine the local concentration distribution is necessary. The mixing itself within porous media has been shown to be complex at high Reynolds numbers ( $Re$ ). As such, the flow is characterized by an initial advection-dominated regime as the flow penetrates the pore network and is followed by a diffusion-dominated regime wherein the molecular diffusion redistributes the scalar more effectively than the advection. The advective regime consists of stretching of the scalar front in longer finger-like structures, particularly where the flow is strongest, and can be defined by the plume's concentration mean, variance, and probability distribution [Bonazzi et al. \(2023\)](#). A thorough overview of current state of research and methods used to solve species transport in porous media can be found in [Dentz et al. \(2023\)](#).

At low  $Re$ , over a short time these structures regress to a more uniform distribution through molecular diffusion. However, even at low  $Re$ , the process of homogenization by diffusion may be retarded by the presence of local chemical heterogeneities in the form of solid adsorbing particles which affect the concentration field. The effect of varying the quantity of uniformly distributed adsorbers within a porous medium was undertaken previously, with two regimes in the evolution of the concentration field

189 identified and the rate at which one regime reaches the other is determined by the  
190 number of adsorbing elements present [Maggiolo et al. \(2023\)](#).

191 The previous investigations cover primarily changes in adsorptivity, usually a static  
192 value, with the values not necessarily reflecting realistic conditions. The geometries  
193 generally tend to be regular, not reflecting in any way a realistic soil sample. We  
194 will extend this characterization by introducing the presence of polydisperse particles  
195 within the packed bed as well as an adsorption rate dependent upon a proposed adsorp-  
196 tion capacity model for the biochar. In addition, we make use of experimental data to  
197 correctly tune the simulations to realistic adsorption rates and determine how these  
198 factors impact the previously identified regimes as well as report additional influences  
199 on the biochar performance. The results are directly compared to experimental data  
200 to assess the predictive accuracy of our model, quantified by breakthrough curves.

## 201 **2 Experiments**

202 The experiments outlined in this section have been undertaken for two purposes.  
203 Experiment 1 was used calculate the adsorption capacity of the biochar which in turn  
204 is an input in the numerical simulations used to compare against experiment 2. The  
205 results for experiment 2 were directly compared to the numerical results to determine  
206 the accuracy of the model used in this work. All experimental information is given in  
207 this section, with the common materials introduced first, followed by each experiment  
208 and its respective results.

209 The adsorption capabilities of two types of biochar were experimentally deter-  
210 mined: wood-chip biochar (WCB) produced mainly from European spruce and  
211 granulated biochar (GB) produced mainly from agricultural seed waste. The wood chip  
212 biochar was produced by Hjelmsäters Fastigheter AB while the granulated biochar was  
213 produced by Skånefrö AB; both companies being based in Sweden. Figure 1 displays

the types of biochar used in the experiments. Alongside the types of biochar, acid-washed glass beads were also used and acted both as an inert, transparent packing material for the biochar and as a control case with minimal to no adsorption.

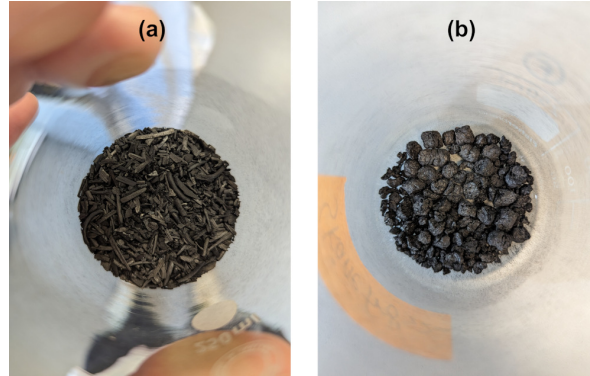


**Fig. 1:** Types of biochar (a) WCB (Hjelsåters Fastigheter AB) and (b) GB (Skånefrö AB).

MB, chemical formula  $C_{16}H_{18}ClN_3S$ , was used as the adsorbate; diluted to 6 mg/L in a phosphate buffer solution containing 380 mg/L  $KH_2PO_4$  and 300 mg/L  $K_2HPO_4$ . It is worth noting that due to its properties, methylene blue can be seen as an analog for some organic pollutants however it is by no means representative of all possibilities. Other compounds or the direct pollutant itself may be required for more accuracy and the numerical model must be appropriately modified as well.

The MB concentration was measured using spectrophotometry with absorbance measured at 680nm. Figure 2 shows the experimental setup that was used for experiments 1 and 2.

## 2.1 Experiment 1

In experiment 1, a known mass of biochar or glass beads (1mm diameter) was placed in a 5cm diameter Plexiglas column, as shown in Figure 3. The quantities of biochar

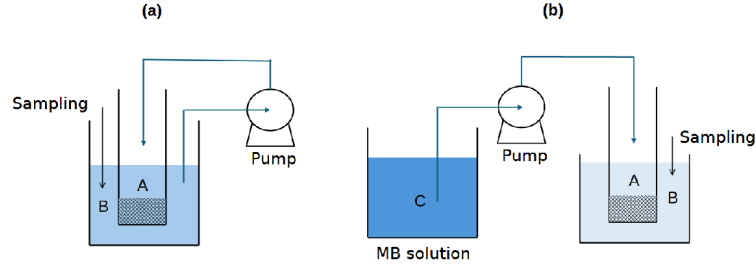


**Fig. 2:** Experimental setup for (a) experiment 1 and (b) experiment 2. A - Inner annular column containing porous medium, B - Outer annular beaker where MB sampling occurs, C - MB reservoir with original concentration  $c_0$  used in experiment 2

were chosen such that differences in behavior would be evident while allowing for a steady-state to be reached within a reasonable time frame.

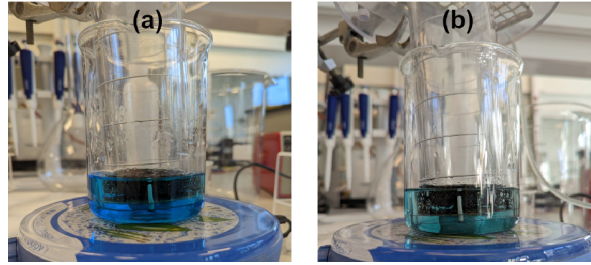


**Fig. 3:** Experiment 1 at (a)  $t = 0$  min and (b)  $t = 135$  min

The bottom of the column was covered with a steel mesh which kept the biochar/glass beads within the column. The column was submerged in a glass beaker containing 100mL of the MB solution, which was circulated through the biochar-packed column using a peristaltic pump operating at a flow rate of 4mL/min. The column is fully immersed in the MB solution to allow for the adsorption to occur at the maximum possible rate, which is a property of the biochar itself rather than a consequence of the local availability of adsorbent. Liquid samples from the solution being circulated through the Plexiglas column were collected regularly from the glass beaker. The quantity of biochar used in this experiment is determined such that the measured difference in adsorbance is clear as the quantity of biochar is increased.

Figure 4 shows the evolution of the normalized outflow concentration over time in experiment 1. Absorbance ( $A$ ) is converted to concentration and normalized against the initial concentration  $c_0$ . We define absorbance as  $A = \log_{10}(I_0/I)$  where  $I_0$  is the intensity of incident light at 680nm wavelength and  $I$  is the transmitted intensity. There is no large difference in the performance for the cases using WCB, even when

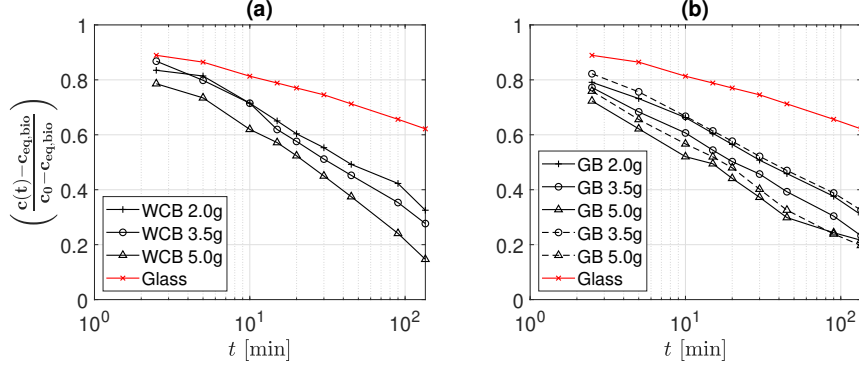


**Fig. 4:** Normalized outflow concentration for (a) Wood chip biochar (WCB), (b) Granulated biochar (GB)

the quantity of biochar is increased to 5 grams; with the results for the GB being similar. To calculate the adsorption capacity of the biochar we employ the conservation equation

$$V_{bio}c_{eq,bio} = V_{liq}(c_0 - c(t_{end})) - V_{glass}c_{eq,glass}, \quad (1)$$

where  $V_{bio}$ ,  $V_{glass}$  and  $V_{liq}$  are the biochar, glass and liquid volumes,  $c_0$  is the initial concentration,  $c$  is the measured concentration, and  $c_{eq,bio}$ ,  $c_{eq,glass}$  are the measured adsorption capacities (equilibrium concentrations) within the biochar and glass, which is the quantity at which they cease to adsorb additional solute, at  $t_{end}$ . Table 1 gives the substrate composition for experiment 1 and the resultant calculated adsorption capacity (equilibrium concentration).

Equation (1) is ideal for calculating the maximum adsorption capacity and biochar equilibrium concentration given that experiment 1 runs until a steady-state is reached,

**Table 1:** Experiment 1, Q = 4mL/min MB solution. WCB - wood-chip biochar, GB - granulated biochar. Calculated adsorption rate  $k = 3.3e - 4$ . [s<sup>-1</sup>]

Material	Glass	WCB			GB				
Weight [g]	20.0	2.0	3.5	5.0	2.0	3.5	3.5	5.0	5.0
$c_{eq}$	0.24	0.42	0.45	0.52	0.43	0.47	0.42	0.48	0.49

257 however this equation is unsuitable for calculating the evolution of the concentration  
 258 at the adsorbing surface over time. To this end we employ the formulation for the  
 259 evolution of the concentration at the adsorber surface

$$-V_p \frac{dc}{dt} = S_p k (c(t) - c_{eq,bio}), \quad (2)$$

$$c(0) = c_0,$$

$$c(t \rightarrow \infty) = c_{eq,bio},$$

260 where the solution takes the form

$$c(t) = (c_0 - c_{eq,bio})e^{-S_p k t / V_p} + c_{eq,bio}, \quad (3)$$

261 where  $V_p, S_p$  are the reactive particle volume and surface area and the adsorption rate  
 262 is calculated by solving (3) for  $k$ , as all other quantities are known. This formulation  
 263 is based upon the assumption that the system is reaction-limited, which is valid since  
 264 the biochar is initially fully immersed in the solution. Fully immersed biochar allows  
 265 for the entire surface area of a reactive particle to contribute in the removal of the MB  
 266 with maximum efficiency, hence reaction-limited. The calculated adsorption rate is  
 267 used in the calibration of the simulations, as explained in section 3.2. It is important to  
 268 mention that the above formulations cannot be used for the analysis of experiment 2 as  
 269 it is mass-transport limited and thus we cannot make any assumption on the evolution  
 270 of adsorption in time. Thus we are forced to model the rate at which the adsorption

271 capacity of the biochar is reached, and it's subsequent effect on the adsorption rate  
 272 itself.

273 If one wishes to apply a simple capacity model to the system, the resulting bound-  
 274 ary condition at the reactive particle surface will be as in equation (4). Note that this  
 275 condition bears striking similarity to (2) but is distinct, supporting our claim equation  
 276 (3) is not suitable for solving the mass-transport limited problem. In these equations  
 277  $D_m$  is the molecular diffusivity,  $Da$  the Damköhler number, and  $f(c)$  the capacity  
 278 model. This condition will be formalized in section 3.2 and is only presented here to  
 279 demonstrate the differences in boundary condition between the experiments.

$$-V_p \frac{dc}{dt} = S_p D_m \frac{\partial c}{\partial n}, \quad (4)$$

$$\begin{aligned} \frac{S_p D_m}{Q} \frac{\partial c}{\partial n} &= \frac{k S_\zeta}{Q} f(c) c(t), \\ &= Da f(c) c^*|_{S_\zeta}. \end{aligned} \quad (5)$$

## 280 2.2 Experiment 2

281 In experiment 2, the Plexiglass column was filled with glass beads mixed with WCB to  
 282 a height of 32mm. The biochar made up 15% of the column by volume and was either  
 283 evenly mixed with the glass beads, placed as a layer at the bottom of the column, or  
 284 placed as a layer at the top of the glass beads. The chosen fraction of 15% is motivated  
 285 by the standard composition used in green roofs in industrial production, which varies  
 286 but provides diminishing benefits beyond this fraction. The column was submerged in  
 287 a beaker filled with approximately 100mL phosphate solution without MB. The MB  
 288 solution was then fed to the top of the column at a flow rate of 8mL/min and the  
 289 MB concentration in the solution surrounding the column was measured in regular  
 290 time intervals. Table 2 outlines the cases shown in Figure 5, including variable particle  
 291 distributions and the equivalent weight of the included biochar.

**Table 2:** Experiment 2,  $Q = 8\text{mL/min}$  with MB solution.  
WCB - wood-chip biochar.

Material Type	%Biochar	Biochar [g]	Particle dist. [mm]
Glass Only	0.0	0.0	$\mu = 1.0$
Glass Only	0.0	0.0	$\mu = 1.0, \sigma = 0.5$
Glass + WCB	15.0	0.93	$\mu = 1.0, \sigma = 0.5$
Glass + WCB	15.0	0.93	$\mu = 1.0, \sigma = 0.5$
Glass + WCB	15.0	0.93	$\mu = 1.0$
Glass + WCB	15.0	0.93	$\mu = 1.0$

The results of experiment 2 are shown in Figure 5 in the form of normalized concentration outflow, also called breakthrough. Once again the data is normalized against an initial concentration. We see an initial period where little of the MB is adsorbed,

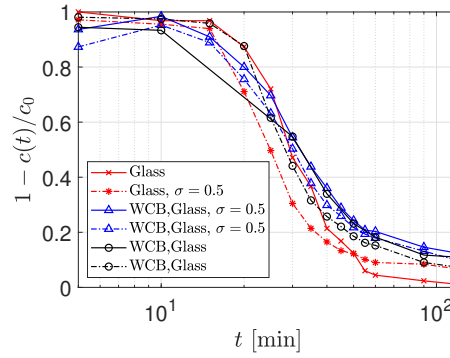


**Fig. 5:** Evolution of concentration breakthrough  $1 - c(t)/c_0$

whereafter the reaction rapidly reaches saturation within the biochar and little additional MB solution is adsorbed, leading to a "steady state" in the breakthrough curve. These periods; the initial adsorption, the rapid saturation, and the ceasing of additional adsorption can be characterized by the time intervals of i)  $0 < t < 20$ , ii)  $20 < t < 70$ , and iii)  $t > 70$ .

We see that the cases using only glass beads perform the worst, as expected. Interestingly these cases also adsorb some measure of MB, which means their behavior should be taken into account when examining the results of the cases which include biochar. Indeed, the inclusion of the quantities of biochar used in these experiments

show that they perform only marginally better than the glass beads themselves. Another important point to note from Figure 5 is that there is little discernible difference between cases in which a variety of particle sizes are present and cases where only a single particle size are used. This will be touched upon later in the numerical simulation results, particularly when the concept of adsorption capacity of reactive particles is present within the system.

## 3 Numerical approach

### 3.1 Lattice Boltzmann method

When one talks about solving the transport of a scalar, we formalize the concept using the advection-diffusion equation

$$\frac{\partial c}{\partial t} = \nabla \cdot (D_m \nabla c) - \nabla \cdot (\mathbf{u}c) + R, \quad (6)$$

where  $c$  is a scalar (in our case concentration),  $t$  is time,  $D_m$  is the diffusion coefficient,  $\mathbf{u}$  is the advecting fluid velocity, and  $R$  is a sink/source term related to reactive processes. At the micro-scale this equation can be represented using the Boltzmann transport equation, which describes motion through particle streaming as well as collisions.

It is an ideal choice for solving flows in porous media due to the complex geometry involved and allows for detailed information of the flow dynamics to be extracted at the pore scale. The system is solved on a lattice structure wherein each lattice element consists of a centroid and nodes placed on a cubic convex hull. The fictive particles travel along the lattice nodes governed by probabilities appropriate for the chosen lattice geometry such that the macroscopic properties of the fluid are preserved [Succi \(2001\)](#). A 3D regular cubic lattice with 19 degrees of freedom for movement (D3Q19)

326 is used and the solved equation is of the form

$$f_r(\mathbf{x} + \mathbf{c}_r \delta t, t + \delta t) - f_r(\mathbf{x}, t) = -\tau^{-1}(f_r(\mathbf{x}, t) - f_r^{eq}(\mathbf{x}, t)) + F_r \quad (7)$$

327 where  $f_r(\mathbf{x}, t)$  is the distribution function at position  $\mathbf{x}$  and time  $t$  along the  $r$ -th  
 328 direction;  $\mathbf{c}_r$  is the so-called discrete velocity vector along the  $r$ -th direction over time  
 329 interval  $\delta t$ ;  $f_r^{eq}$  is the equilibrium distribution function; and  $\tau$  is the mean collision time  
 330 and is related to kinematic viscosity by  $\nu = c_s^2(\tau - 0.5\delta t)$ . The equilibrium distribution  
 331 function  $f_r^{eq}(\mathbf{x}, t)$  takes the form

$$f_r^{eq} = w_r \rho \left( 1 - \frac{\mathbf{u} \cdot \mathbf{u}}{2c_s^2} \right), \quad r = 1 \quad (8)$$

$$f_r^{eq} = w_r \rho \left( 1 + \frac{\mathbf{c}_r \cdot \mathbf{u}}{c_s^2} + \frac{(\mathbf{c}_r \cdot \mathbf{u})^2}{2c_s^4} - \frac{\mathbf{u} \cdot \mathbf{u}}{2c_s^2} \right), \quad r = 2 - 19 \quad (9)$$

332 where  $w_r$  is the appropriate weighting parameter for the D3Q19 lattice;  $\rho$  is the den-  
 333 sity;  $c_s$  is the speed of sound; and  $\mathbf{u}$  is the velocity used for defining the equilibrium  
 334 distribution functions, which can differ from the fluid hydrodynamic velocity, on the  
 335 basis of the specific forcing scheme used.

336 The macroscopic flow quantities density and velocity,  $(\rho, \mathbf{u})$  are thus related to the  
 337 hydrodynamic moments as the following:

$$\rho = \sum_r f_r, \quad (10)$$

$$\rho \mathbf{u} = \sum_r \mathbf{c}_r f_r + \frac{\Delta t}{2} \left( \frac{\Delta P}{L} \right), \quad (11)$$

338 where  $\Delta t = 1$  in our case. The force  $F_r$  as formulated by [Guo et al. \(2002\)](#) is applied  
 339 to the fluid, which mimics the flow rate intensity during a rain event in our case as

described later in more detail, and is given by

$$F_r = \left(1 - \frac{1}{2\tau}\right) w_r \left( \frac{\mathbf{c}_r - \mathbf{u}}{c_s^2} + \frac{\mathbf{c}_r \cdot \mathbf{u}}{c_s^4} \mathbf{c}_r \right) \left( \frac{\Delta P}{L} \right). \quad (12)$$

### 3.2 Solute adsorption implementation

A solute adsorption rate is assigned to a percentage of chosen particles  $\zeta$  such that their surfaces  $S$  follow the first-order kinetics given by:

$$-\frac{\partial c^*}{\partial \lambda_s^*}|_{S_\zeta} = \text{Da } c^*|_{S_\zeta}, \quad (13)$$

where  $\text{Da}$  is the Damköhler number,  $c^* = c(\mathbf{x}, t)/c_0$  is the dimensionless concentration at position  $\mathbf{x} = (x, y, z)$ , and  $\lambda_s^* = \lambda_S/d$  is the dimensionless direction pointing inward to the particle surface. The Damköhler number, a ratio of the reaction rate and the advective mass flow rate, is given by

$$\text{Da} = kS_\zeta/Q, \quad (14)$$

where  $k$  is the adsorption rate on the particle surface,  $S_\zeta$  is the total reactive surface area expressed as a fraction  $\zeta$  of the total particle surface area, and the flow rate is given by  $Q = l_0^2 \varepsilon U$ . Here  $l_0$  is the porous domain width,  $\varepsilon$  is the porosity, and  $U$  is the mean streamwise velocity.

Numerically, the concentration field  $c(\mathbf{x}, t)$  is solved using a second population which is transported by the fluid velocity  $\mathbf{u}$ . The solute is then initialized at the inlet of the porous media as a volume with concentration  $c_0$ . The second lattice population,

denoted  $g_r$ , gives the local concentration field by

$$c(\mathbf{x}, t) = \sum_r g_r(\mathbf{x}, t). \quad (15)$$

We impose a Neumann boundary condition at the adsorbing surfaces for the scalar lattice Boltzmann quantity  $g_r$ . The distribution function at a fluid node  $\mathbf{x}$  in the proximity of an adsorbing surface placed at  $(\mathbf{x} - \mathbf{c}_r)$  is corrected along the wall-normal direction  $r$  as

$$g_r(\mathbf{x}, t + 1) = \frac{-A_1 + A_2}{A_1 + A_2} g_r(\mathbf{x}, t) + \frac{2w_r A_3}{A_1 + A_2}, \quad (16)$$

where  $A_1 = k$ ,  $A_2 = D_m$ , and  $A_3 = 0$ . This condition was developed by [Huang and Yong \(2015\)](#); [Huang et al. \(2016\)](#).

In order to limit the reactivity as the particle surface reaches high levels of concentration we apply a functional coefficient to the prescribed reaction rate. This limit is designed to act as an analog to the particles reaching a saturated state wherein they can no longer adsorb more of the solute, known as adsorption capacity. Several different functions were tested, including a triangular function as well as a sigmoid function however a simple linear function was chosen, of the form

$$f(c) = 1 - c/c_{eq}, \quad \forall c \leq c_{eq} \quad (17)$$

which allows for full reactivity at low values of concentration but reaches zero when the particle equilibrium concentration has been reached. This equilibrium concentration is set to  $c_{eq} = 0.5$  and is based upon the results of experiment 1. This alteration is reflected in the adsorption boundary condition, becoming

$$-\frac{\partial c^*}{\partial \lambda_s^*}|_{S_\zeta} = \text{Da } f(c)c^*|_{S_\zeta}, \quad (18)$$

372 which is the equivalent of equation (4) presented in the previous section.

### 373 3.3 Domain generation and operating conditions

374 The pore structure used in the simulations is a packed bed generated by the applica-  
375 tion of rigid body physics on falling spheres within a cylindrical container. Two such  
376 cases are generated; i) a monodisperse case with a fixed particle diameter, and ii) a  
377 polydisperse case with the mean diameter equal to that of the monodisperse case. The  
378 particles are centered around a diameter of 1.0 with  $2\sigma = \pm 0.82$  millimeters. A cubic  
379 subdomain is then selected from the cylindrical container and the volume is discretized  
380 into a binary matrix of  $l_0^3 = 256^3$  computational nodes, giving the mean particle diam-  
381 eter  $d = 21.6$  nodes. The method by which the domain is generated and characterized  
382 can be found in [Maggiolo et al. \(2023\)](#) such that domain integrity is assured and the  
383 volumetric porosity is calculated to be  $\varepsilon = 0.4, 0.36$  for the mono- and polydisperse  
384 cases, respectively.

385 In order to simulate an intense rainfall event the Péclet number  $Pe > 1$  and we  
386 assume little inertial influence, thus  $Re < 1$ . We set the Damköhler number,  $Da \approx 1$ ,  
387 which represents equal magnitudes of molecular diffusion and reaction rates, as calcu-  
388 lated in the experiment 2. By applying the conditions required above, the simulation  
389 has  $Re = 0.017$  and  $Pe = 6.7$ , which is representative of a rainfall event with intensity  
390 of around 60mm/hr. The flow rate of experiment 2 is  $Q = 8\text{mL/min}$ , which converts  
391 to about 600mm/hr, about double the world record rainfall intensity, with  $Pe = 250$   
392 and  $Re = 0.17$ . It is worthwhile to note that intensities higher than the record can be  
393 reached when runoff is channeled to a porous surface, which is not naturally occur-  
394 ring rainfall. While these values are higher than those chosen for the simulation, the  
395 governing physics are identically balanced, as the originally defined conditions are all  
396 satisfied, including  $Da \approx 1$ . With the above mentioned flow rates we have been able  
397 to measure variations in concentration quantities in a few hours, which we found as a

398 good time lapse to minimize effects from changes in environmental conditions on the  
399 measurements.

400 These conditions are used to tune  $\Delta P/L$ , the molecular diffusivity and viscosity  
401 accordingly. It is worth mentioning that common rainfalls are between 3-8mm/hr,  
402 however less common extreme events can reach 15-60 mm/hr or more. We can extrap-  
403 olate the simulation conditions to lower rainfall intensities by accounting for the time  
404 scale of the physical processes involved. The soil will not be as thin as that in the  
405 simulations and no runoff infiltration front will be pure contaminant. Additionally,  
406 one can alter the diffusivity to compensate such that the physically realistic process  
407 is retained.

408 The resultant mean flow velocity is averaged over the entire domain, given by  
409  $U = (\int_{l_0^3} u_z dl_0^3) / l_0^3 \varepsilon$ . The Kozeny-Carman relationship stipulates that if the porosity  
410 of a domain is altered the flow rate must be changed accordingly. Since in our cases  
411 porosity is approximately unaltered, the resultant mean velocity for the polydisperse  
412 case is the same. The biochar percentage is set to 30% in the simulations, double the  
413 industry maximum recommendation, to improve statistical analysis on single particle  
414 adsorption features without straying significantly from realistic conditions.

415 The initial concentration  $c_0 = 1.0$  is applied to an inlet zone directly adjacent to  
416 porous volume. The streamwise boundaries are assigned a periodic condition wherein  
417 buffer zones are applied to the inlet and outlet boundaries to prevent any effect on the  
418 flow within the porous zone. The lateral boundaries are assigned a free-slip condition.

419 The simulations are run in two steps; first the single phase velocity profile is solved  
420 for each geometry and then the solute is added. In this way we solve only the steady-  
421 state flow in the first stage and only the concentration profile in time in the second  
422 stage. Six cases total are run on two different geometries, the details of which can be  
423 found in Table 3.

**Table 3:** Case numbers corresponding to operating conditions. Adsorption rate, particle type, and adsorption capacity are altered between cases.

Case	$k$	Particle	Capacity
1	0.0	Mono	None
2	0.0	Poly	None
3	5.3e-6	Mono	Unlimited
4	5.3e-6	Poly	Unlimited
5	5.3e-6	Mono	Limited
6	5.3e-6	Poly	Limited

## 4 Results

### 4.1 Concentration profiles

We show a comparison of the concentration profile in the domain between the monodisperse and polydisperse geometries for all cases listed in Table 3.

Transverse cuts at  $x/l_0 = 140/256$  are shown at the same timestep  $t^* = 0.6$ , given by  $t^* = tU/l_0$ , which corresponds to the time at which the majority of the reactive particles begin to reach their full capacity, in the cases with limited capacity. Particles marked with black stars indicate reactive particles. Figures 6(a), (c), and (e) display a more homogeneous front, all with the monodisperse geometry. We do see decreased homogeneity in figures 6(b), (d), and (f), where we have the polydisperse geometry. One can see clearly the difference in front homogeneity and indeed the formation of tendrils of higher concentration within these figures. We also observe a general trend of decreased homogeneity in the polydisperse cases with adsorption, (d) and (f), which we investigate in more detail in subsequent sections.

### 4.2 Average surface concentration and flux ratio comparison

The average surface concentration of all reactive particles is given in Figure 7. This quantity is calculated by summing the concentration on all particle surface nodes and dividing by the total amount of such nodes. In Figure 7(a) there is a great similarity

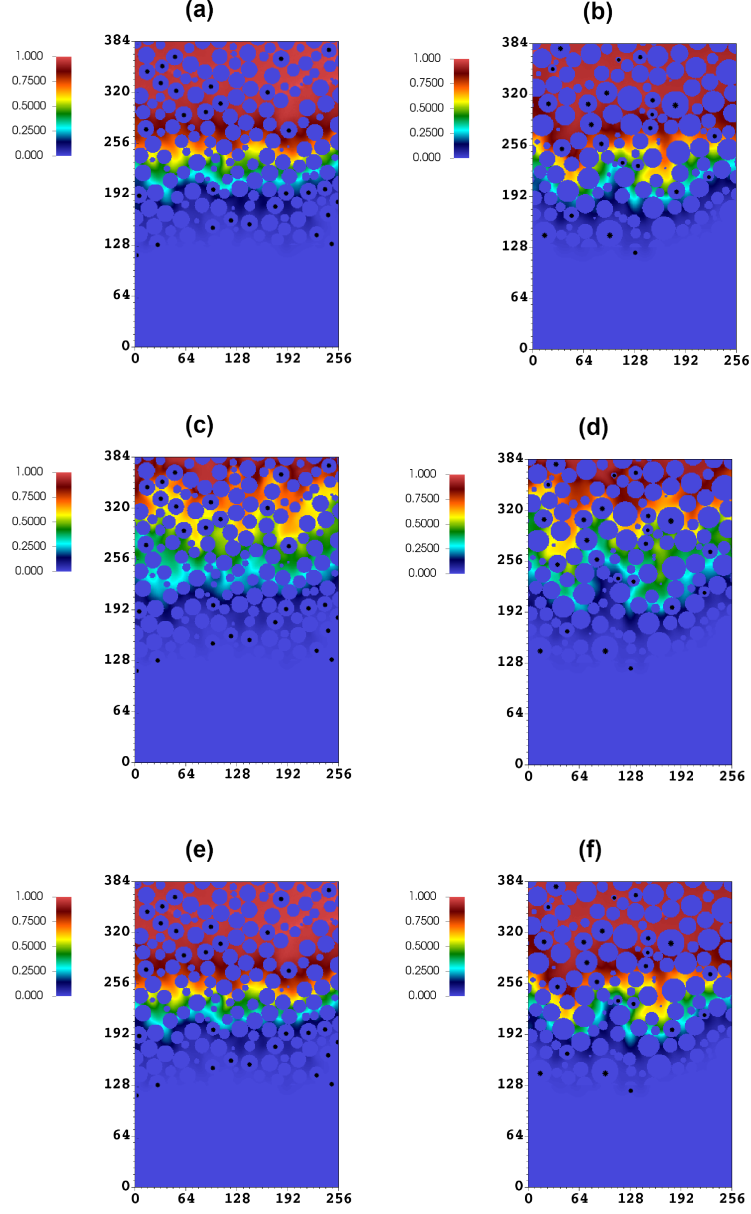


**Fig. 6:** Concentration profiles cut at  $x/l_0 = 140/256$  and  $t^* = 0.6 \approx 20$  min. Black stars indicate reactive particles. No capacity: (a) Case 1, (b) Case 2. Unlimited capacity: (c) Case 3, (d) Case 4. Limited capacity: (e) Case 5, (f) Case 6. The polydisperse cases (right panels) appear to generate a less homogeneous concentration front.

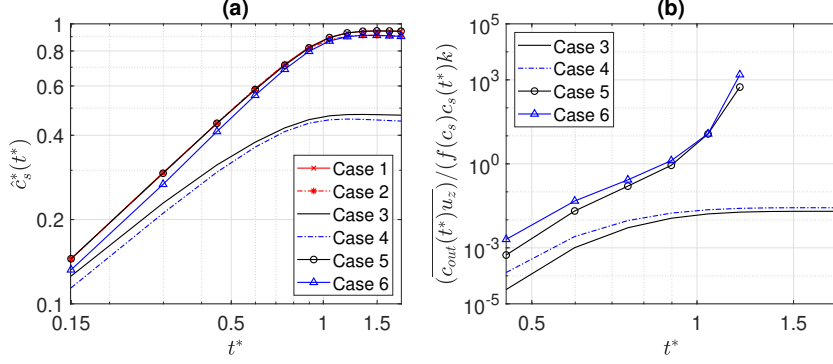


**Fig. 7:** (a) Average surface concentration and (b) breakthrough flux/adsorption flux ratio as a function of dimensionless time. No capacity: Case 1,2. Unlimited capacity: Case 3,4. Limited capacity: Case 5,6

of behavior between the cases with no capacity and those with a limited adsorption capacity. We see the surface concentrations increase to near unity as the reactive particles are no longer capable of removing more solute from the liquid. On the other hand, if one examines the cases with unlimited capacity we see a significantly reduced surface concentration, around 0.5. This is their effective equilibrium state and further reduction or buildup will not occur without external stimulus. We also note that there is little difference between the monodisperse and polydisperse geometries, implying a similar total reactive surface area despite the difference in individual particle surface areas, which is the case.

In Figure 7(b) the ratio of the breakthrough flux and the adsorption flux is shown. This quantity can be seen as a measure of the medium leakage reduction as a consequence of biochar adsorption. Note that the cases with the limited capacity model end prematurely due to the particles ceasing to adsorb after reaching their adsorption capacity. The ratio in the beginning of the simulations is extremely small, indicating adsorption is the dominant flux in the system, however this reduces significantly as the simulations progress. This is expected since the concentration flux at the outlet will increase over time as the solute travels through the medium. At longer times the

ratio for the unlimited capacity cases stabilizes at around  $10^{-2}$  indicating an equilibrium between the adsorption and the breakthrough flux throughout the simulation lifetime. This is not true in the cases with limited adsorption capacity, wherein we see an inflection point at which the particles cease to react and the breakthrough flux quickly becomes the only contributing factor. This period of approaching particle inertness is quite similar for both geometries, indicating a negligible effect of the front homogeneity on this macroscopic quantity.

### 4.3 Breakthrough curves (vs. experiments)

Breakthrough curves are calculated for all cases and displayed in Figure 8 where (a) is the average concentration present in a small outlet volume the thickness of one particle diameter calculated as

$$\overline{c_{out}(t^*)u_z} = \left( \int_{V_{out}} c_{out}(t^*)u_z dV_{out} \right) / V_{out} \quad (19)$$

where  $V_{out} = l_0^2 \varepsilon d$  and (b) illustrates the comparison of like cases between the experimental results and the simulations. In these graphs, a value of 1 represents a full

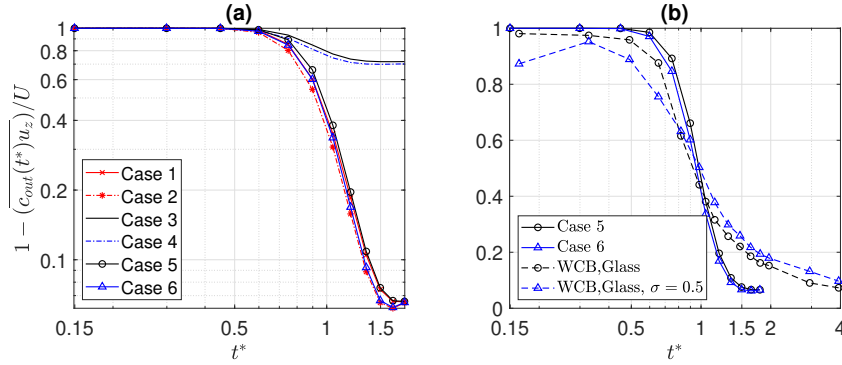


**Fig. 8:** Breakthrough curves for (a) simulation and (b) between like experimental cases and simulations. 1 - no solute reaches outlet, 0 - no adsorption has occurred, all solute reaches outlet. No capacity: Case 1,2. Unlimited capacity: Case 3,4. Limited capacity: Case 5,6

471 reaction wherein nothing reaches the outlet and 0 represents no change in concentra-  
472 tion between inlet and outlet, i.e. nothing has been removed. It is immediately clear  
473 in Figure 8(a) that unlimited capacity cases perform significantly better in terms of  
474 leakage than those which have a limit or have no reactivity. Interestingly, there is lit-  
475 tle difference in performance between the cases with no adsorption capacity and those  
476 with limited capacity. This is due to the fact that the limited capacity particles reach  
477 capacity very swiftly and thus contribute very little to removing the solute after the  
478 earlier stages of the simulation.

479 This hypothesis is given some weight by Figure 8(b) where two experimental cases  
480 are directly compared to the simulation cases with limited adsorption capacity. We  
481 find a very similar behavior in that both experiments and simulations swiftly reach  
482 capacity and subsequently remove little of the solute. Note that there is an initial  
483 period of time for the MB solution to reach the porous media through the piping and  
484 we do not take wall effects into account in the simulation; both of which are present in  
485 the experiment. Consequently, the experimental curves have a lower gradient and take  
486 additional time to reach full capacity, however the steady-state behavior is correctly  
487 reflected by the simulations.

488 At lower rainfall intensities we expect to see an increased residence time of the  
489 adsorbent near the biochar surfaces, however this will not matter if the biochar is  
490 already at capacity. In addition to the uncertain reaction kinetics, lower rainfall inten-  
491 sities may also result in unsaturated flow conditions, radically altering the system and  
492 introducing capillary forces, making any prediction based upon the current work void.  
493 Finally, a lower flow velocity may transition from more complex mixing caused by the  
494 microstructure to a more simplified laminar flow in larger pore spaces.

#### 4.4 Flow homogeneity and outlet flow profile

We examine the probability distribution for the streamwise and transverse velocity magnitude as a quantification of the flow homogeneity within each geometry as well as compare between the two.

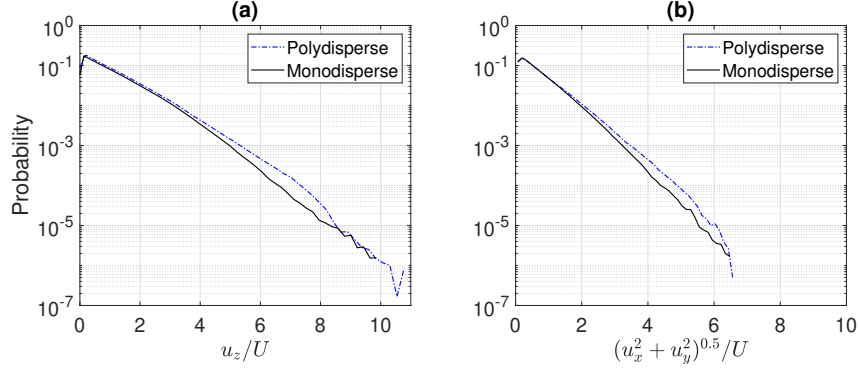


**Fig. 9:** Probability distribution of the domain velocity with (a)  $u_z/U$  where  $u_z$  is the streamwise velocity component and (b)  $(u_x^2 + u_y^2)^{0.5}/U$  the transverse velocity magnitude

Figure 9(a) shows the normalized streamwise velocity and it is clear that the streamwise velocity is largely similar to that of the mean velocity. However, variations up to 10 times that value exist within the flow field which is also reflected in the distribution of the transverse velocity. There is no real discernible difference in the distributions between the two geometries, thus we can be reasonably confident that the flow alone is not a primary factor in notable differences observed between cases. Indeed, we do see increased inhomogeneity induced by increased adsorption in the front profiles shown in Figure 6.

Figure 10 displays the probability distributions for the breakthrough flux, measured  $c(t^*)u_z/U$ , as a quantification of the flow homogeneity at the outlet. This gives an indication of how the flow interacts with the reactive particles, producing tendrils

of increased concentration as opposed to a more uniformly distributed concentration front.

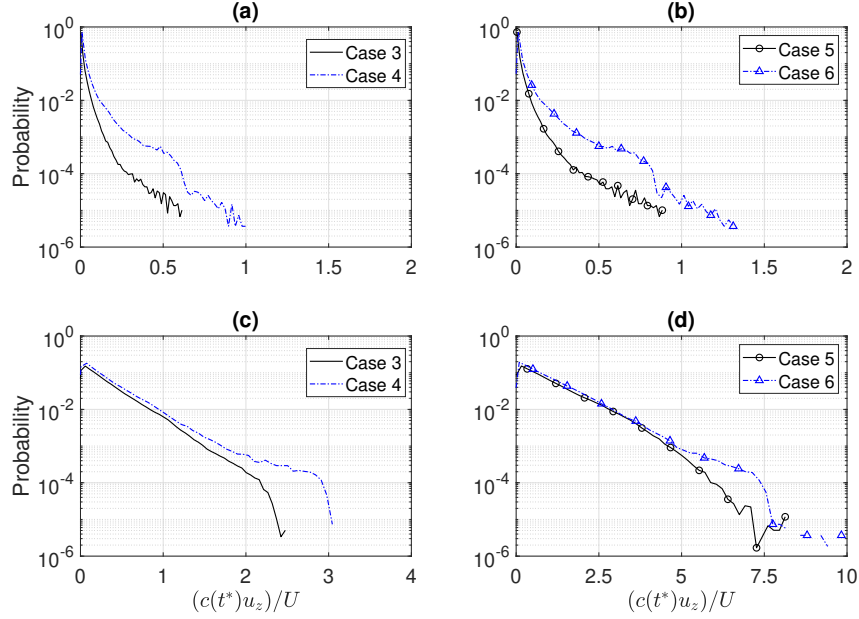


**Fig. 10:** Breakthrough flux distributions for (a) Unlimited capacity,  $t^* = 0.6$  (b) limited capacity,  $t^* = 0.6$  (c) Unlimited capacity,  $t^* = 1.5$  (d) limited capacity,  $t^* = 1.5$

511

512 We compare the distributions during the period where the solute first reaches the  
 513 outlet ( $t^* = 0.6$ ), figures 10(a) (unlimited capacity) and 10(b) (limited capacity) and  
 514 when the steady state at the outlet is reached ( $t^* = 1.5$ ), figures 10(c) (unlimited)  
 515 and 10(d) (limited). A value near 1 indicates tendrils of high concentration trans-  
 516 ported at a velocity around that of the streamwise mean velocity. Deviations from  
 517 this imply a change to the local concentration or streamwise velocity. In other words,  
 518 fluctuations around the mean of the concentration flux. Note a strong similarity in dis-  
 519 tribution between 10(a) and 10(b), though the measured concentration flux is slightly  
 520 higher in the limited capacity case. In all cases the monodisperse geometry exhibits  
 521 a lower and tighter distribution of outflow concentration, indicating higher and more

522 efficient adsorption of the solute. The largest deviation is found in Figure 10(d), which  
 523 compared to the unlimited capacity case in 10(c), has a higher concentration flux mag-  
 524 nitude. We know from our analysis of the flow itself there is little influence on the flow  
 525 induced by each geometry, thus the adsorption rate spatial distribution is the likely  
 526 cause for this phenomenon.

## 527 4.5 Particle adsorption capacity

528 Figure 11 displays the PDFs of average particle surface concentration  $c_s^*$  during the  
 529 transition stage  $t^* = 0.6$ , figures 11(a),(b) wherein particles are reaching their capacity  
 530 and begin to become non-reactive. The lower figures, (c),(d) show the same cases,  
 531 however the timestep is altered to reflect the steady-state distribution found at  $t^* =$   
 532 1.5. Figures 11(a),(c) are unlimited capacity and (b),(d) are limited capacity. The  
 533 order of cases and times is replicated for Figure 12.

534 Figure 12 displays PDFs for the surface concentration flux  $c_s^* S_p / S_\mu$ , using the  
 535 prefactor  $S_p / S_\mu$ , where  $S_p$  is individual particle surface area and  $S_\mu$  is mean particle  
 536 surface area. This ratio is the measure of the available adsorptive surface area com-  
 537 pared to that of the ideal surface area of a representative particle. When combined  
 538 with a particle's surface concentration we can get an idea of which particles are more  
 539 effective individually in terms of the adsorptive flux.

540 In Figure 11 we show the distribution of each particles' average surface concentra-  
 541 tion, taken at an intermediate and steady-state time. We observe no notable differences  
 542 between the monodisperse and polydisperse geometries. At the intermediate time the  
 543 distribution for the limited capacity cases exhibits the U-shaped distribution typi-  
 544 cal of diffusion-dominated systems, with two peaks at the extrema. In the cases with  
 545 unlimited reactivity the peak at higher concentration disappears due to the contin-  
 546 uous adsorption, figure 11(a). At the steady-state, the cases with limited adsorption

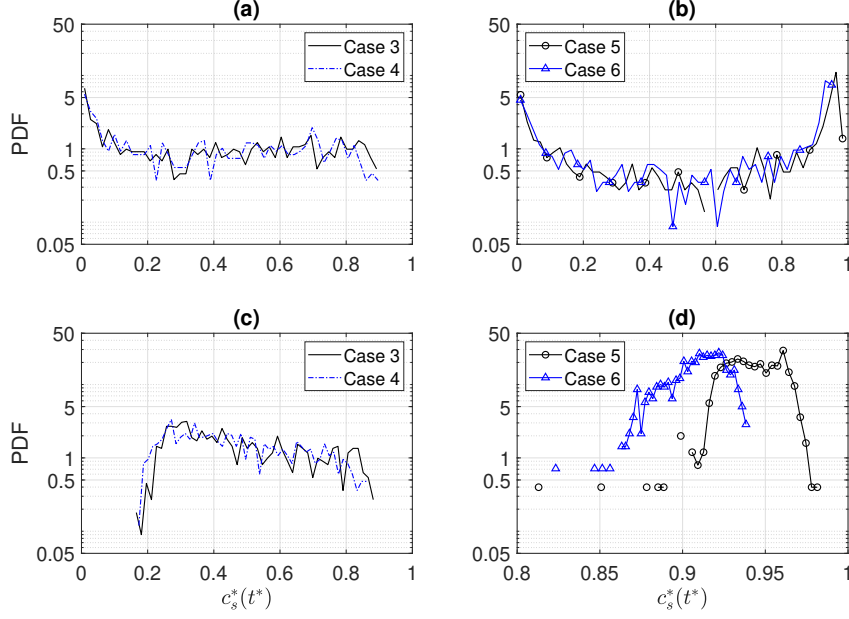


**Fig. 11:** Particle average surface concentration PDFs for (a),(b)  $t^* = 0.6$  and (c),(d)  $t^* = 1.5$ . Unlimited capacity: Case 3,4. Limited capacity: Case 5,6

tend towards concentration of 1 with a very narrow distribution of values whereas the unlimited are more widely distributed, figures 11(c),(d).

When one examines the surface concentration flux  $c_s^* S_p / S_\mu$  in the cases with unlimited capacity, figures 12(a),(c), we observe a similar behavior to that of the average particle surface concentration. As expected, a similar trend is also evident in the monodisperse case with limited capacity, figures 12(b),(d), when compared to the distribution evolution in time of figures 11(b),(d). Indeed  $S_p / S_\mu \approx 1$  in the monodisperse case.

This is not reflected in the polydisperse case with limited capacity. At longer times where the concentrations are uniformly  $c_s^* \approx 1$ , the fluxes will tend to the distribution of  $S_p / S_\mu$ , figure 12(d). Due to the fact that the particle radii are normally distributed, the probability of  $S_p / S_\mu$  will be  $\chi^2$  distributed, exhibiting an exponential decay away from the mean.

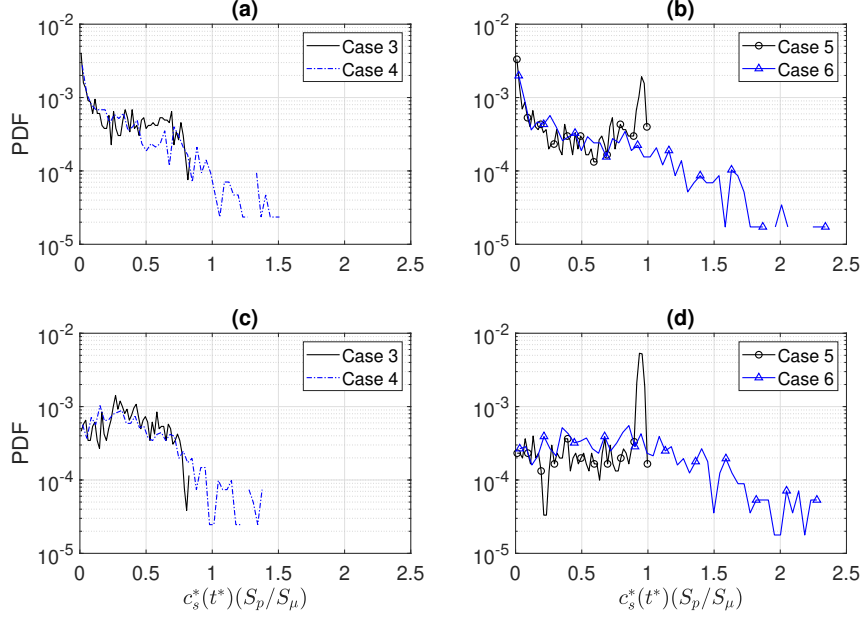


**Fig. 12:** Surface concentration flux PDFs for (a),(b)  $t^* = 0.6$  and (c),(d)  $t^* = 1.5$ . Unlimited capacity: Case 3,4. Limited capacity: Case 5,6

**Table 4:** Ratio of mean particle size with concentration higher than concentration threshold vs. mean particle size of the rest at  $t^* = 0.6$

Concentration	0.3000	0.5000	0.7000	0.9000
Ratio of means	0.9924	0.9908	0.9515	0.8853

560 Interestingly, at the intermediate time, the distribution of the fluxes preserves the  
561 peak at low concentration whereas the peak at higher concentration visible in the  
562 monodisperse case here is absent for the polydisperse case. We calculate the ratio of  
563 mean particle size with concentration higher than a certain threshold against the mean  
564 size of the remainder particles, shown in Table 4. It is noticeable that high surface con-  
565 centrations, that is above a specified threshold, are found on smaller particles. In turn  
566 the distribution of fluxes ( $c_s^* S_p / S_\mu$ ) decreases uniformly as the flux itself increases,  
567 figure 12(b). This may indicate that some particles in the polydisperse geometry are

being underutilized. If one examines the cuts shown in Figure 6 where the polydisperse cases display preferential pathing we see some occurrences of preferential paths probably following high concentrations around smaller particles which have reached capacity.

The behavior discussed above regarding the monodisperse geometry is indicative of a more homogeneous front, where the particles are either being approached by the front or are surrounded by it, whereas the front reaches the particles in the polydisperse geometry at different times, leading to a higher distribution of different magnitudes. We note that the monodisperse case exhibits an overall higher surface concentration at the steady-state than that of the polydisperse cases. This is coupled with a similarly lower breakthrough flux. One explanation for this is the increased inhomogeneity observed in the concentration profiles for the polydisperse geometry. This preferential pathing by the formation of tendrils of higher concentration removes solute from reaching particles that would otherwise aid in the removal of concentration from the flow. This channeling effect reduces the efficiency of the reactive particles as some available surface area is left unused, effectively underutilizing them. A more homogenous front allows for the maximum surface area to be reached at any given time.

Figure 13 shows the particle diameter and surface area distributions to aid in the interpretation of the results as discussed above. Figure 13(a) shows the distribution of reactive particles only and all particles for the polydisperse case as well as the resultant normal distribution curve. The distribution of dimensionless surface area is shown in Figure 13(b) for the polydisperse case only. It is compared to the ideal PDF of diameter squared  $d^2$  which follows a  $\chi^2$  distribution. The difference observed are due to surface contact or cutting along the domain edges. Despite this fact, we are satisfied that the distributions shown here justify the discussion we have entertained regarding geometry effects and the potential for preferential pathing induced by the polydisperse geometry in particular.

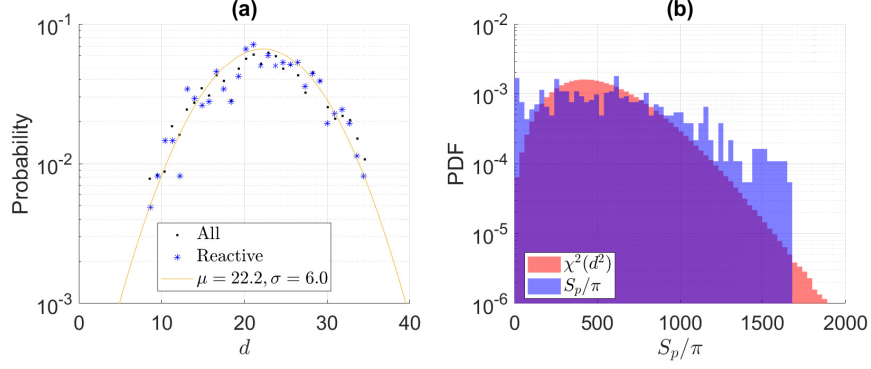


**Fig. 13:** (a) Particle diameter  $d$  distribution in l.u.. Dots indicate all domain particles, stars are just reactive particles. Line is the normal distribution function with  $\mu = 22.2, \sigma = 6.0$ . (b) PDF of reactive particle surface area  $S_p/\pi$  (blue),  $\chi^2(d^2)$  distribution of particle diameter  $d$  (red)

We can now state with reasonable certainty that reactive particles do influence the concentration profiles, particularly the available reactive surface area. An advantage may be achieved by using more monodisperse particles, as they promote a more homogeneous front for the advancing solute and reduce the solute leakage, particularly in the case of particles with limited adsorbing capacity.

#### 4.6 Modifying the reaction kinetics

We close the paper with a short discussion on the practicalities of accurately modelling the adsorption dynamics present in reality on the surface of biochar. There are several different mechanisms by which adsorption occurs; namely pore-filling, hydrophobic interaction, surface complexation, electrostatic interaction, hydrogen bonding interaction,  $\pi - \pi$  electron-donor-acceptor (EDA) interaction, and intra-particle diffusion. In addition it has been shown that thermal conditions as well as the pH of the environment play a non-negligible role in the reaction speed [Ji et al. \(2024\)](#); [Gupta et al. \(2020\)](#), as does aging or the presence of dissolved organic matter. The sum total of considering individual biochar characteristics, their intrinsic modes of adsorption, as well as environmental factors renders the modelling a significant challenge. In general

current works have made use of first and second order pseudo-kinetic models alongside Langmuir and Freundlich isotherms. Some forays have been undertaken in the realm of applied artificial neural networks and statistical chemical modelling however this is still in its infancy for such an application. If one wishes to enhance the models governing the reaction kinetics we need more experimental data to determine which of the above modes of adsorption should be considered and how the environmental and aging aspects can be included in the models. While some kind of pre-factors can be easily applied they are not representative of any physical phenomenon and some possible empirical model must be constructed which accurately captures these effects may be a simple and efficient solution. Alternatively the full chemical species and reactions can be included in the modeling but this undertaking may not be compatible with how the lattice Boltzmann method operates but would ensure a more chemically consistent interaction. Pore filling and intra-particle diffusion might be handled via some volumetric functions that account for internal pore volume and pore network but this is also impractical to implement. Whichever strategy is used, more experimental data is likely to be required and understanding the fundamental physical interactions in such a system are a good place to aid in determining where to next add the increased realism required for more accurate and applicable predictions.

## 5 Conclusion

Experiments have been undertaken to determine the adsorption rate and capacity of two different kinds of biochar alongside breakthrough curves for same. The breakthrough curves are calculated using the absorbance of an MB solution over a period of time. Simulations are run using the experimental data and a comparison is made between the predicted breakthrough curves and the experimental results, with good agreement found.

636 A deeper investigation of the underlying factors determining the concentration field  
637 evolution is described. This analysis consists of flow velocity and breakthrough con-  
638 centration profiles, average and individual surface concentration distributions, particle  
639 capacity distributions, and a flux ratio comparison. The results show that the flow  
640 velocity distribution remains the same for both simulated geometries, implying that  
641 the differences in concentration distribution may not be a result of the flow velocity  
642 profile. Examination of the breakthrough curves and individual particle concentra-  
643 tion distributions show that the polydisperse geometry promotes preferential pathing  
644 throughout the medium and leads to a more varied distribution of particle states  
645 than those found in the monodisperse cases. This preferential pathing is undesirable  
646 in the context of removal of contaminants from the flow, as a more homogeneous  
647 front ensures the randomly distributed reactive particles will interact with the solute,  
648 whereas tendrils may bypass them entirely and flow directly for the outlet.

649 We have chosen to use spherical packed beds over a realistic soil substrate geom-  
650 etry due to the intrinsic inhomogeneity found within soil scans taken using x-ray  
651 microtomography (XMT) or any similar technique. A chosen domain may contain few  
652 very large particles and multitudes of tiny particles or anywhere in between, rendering  
653 the porosity of any such domains fluctuating wildly, making comparisons difficult. In  
654 future it is worthwhile to determine if the trends observed in this work hold true for  
655 the realistic soils as well.

656 If one extends these results to application recommendations, we can state that  
657 the observed differences between the mono- and polydisperse cases are larger than  
658 those observed when biochar is present or not. This would correspond to cases 1  
659 and 2 (no biochar) and 5 and 6 (biochar with a limited capacity). The concept of  
660 limited adsorption capacity is analogous to the realistic adsorbance occurring in the  
661 experimental biochar, which cannot remove the solute indefinitely. These cases only  
662 slightly outperform the cases in which there are no reactive particles present. This

663 is due to the rate at which the limited capacity particles reach capacity and become  
664 inert. Cases 3 and 4 have unlimited capacity, which one could say is analogous with  
665 roots or some other living biological matter that does not have a capacity in the same  
666 manner as biochar.

667 The practical implication here is that monodisperse beds are preferred as they pro-  
668 mote more even distribution of the solute within the domain and thus allow the random  
669 adsorbers to act with maximum effect, i.e. reaction-limited. Additionally, the presence  
670 of adsorbers with an unlimited adsorption capacity must be taken into account as this  
671 can dramatically effect the results, particularly in proximity to each other. This effect  
672 will obviously increase if the adsorption rate is increased.

673 If one wishes to increase the efficacy of biochar, a high absorptive rate with a  
674 similarly high capacity will greatly reduce breakthrough. This can be accomplished  
675 by modifying the material itself and/or increasing the total quantity of biochar within  
676 the soil, which will consequently increase its capacity. Current practice suggests no  
677 more than 15% biochar by volume is beneficial given common rainfall quantities;  
678 however our results show that performance can be increased if one takes into account  
679 the factors mentioned above, with the additional mention of total reactive surface  
680 area and the idea of induced preferential pathing. Lower rainfall intensities will cause  
681 higher residence time of the concentration front near the biochar; however once they  
682 saturate, which we show can take place quite quickly, breakthrough will still occur.  
683 Thus a more accurate method for modeling the capacity of different adsorbers should  
684 be investigated to improve the predictive ability of the models. Finally, given that  
685 monodisperse particles promote a more homogeneous concentration front and that  
686 total reactive area matters more than individual particle size we suggest that more  
687 uniform sized substrates are used.

688 **Acknowledgements.** This work was supported by the Swedish Research Council  
689 for Environment, Agricultural Sciences and Spatial Planning (FORMAS), Grant No.

690 2019–01261. The computations were enabled by resources provided by the Swedish  
691 National Infrastructure for Computing (SNIC), partially funded by the Swedish  
692 Research Council through Grant Agreement No. 2018–05973.

## 693 References

- 694 Aguilar Fajardo, A.C., Bacchi, G., Cusicanqui Lopez, J.A., Gilardi, G., Maggetti, D.,  
695 Tommasi, L.: Green roof benefits and technology assessment. a literature review.  
696 New Metropolitan Perspectives **482 LNNS**, 1937–1946 (2022) [https://doi.org/10.](https://doi.org/10.1007/978-3-031-06825-6_186)  
697 [1007/978-3-031-06825-6\\_186](https://doi.org/10.1007/978-3-031-06825-6_186)
- 698 Afroze, S., Sen, T.K., Ang, H.M.: Adsorption performance of continuous fixed bed  
699 column for the removal of methylene blue (mb) dye using eucalyptus sheathiana  
700 bark biomass. Research on Chemical Intermediates **42**(3), 2343–2364 (2016) [https:](https://doi.org/10.1007/s11164-015-2153-8)  
701 [//doi.org/10.1007/s11164-015-2153-8](https://doi.org/10.1007/s11164-015-2153-8)
- 702 Bonazzi, A., Dentz, M., Barros, F.P.J.: Mixing in multidimensional porous media:  
703 A numerical study of the effects of source configuration and heterogeneity.  
704 Transport in Porous Media **146**(1-2), 369–393 (2023) [https://doi.org/10.1007/](https://doi.org/10.1007/s11242-022-01822-3)  
705 [s11242-022-01822-3](https://doi.org/10.1007/s11242-022-01822-3)
- 706 Bashir, M., Mohan, C., Annachhatre, A.P.: Regeneration of copper-loaded pine bark  
707 biochar using simultaneous bio-sulfide precipitation of copper. Aqua Water Infras-  
708 tructure, Ecosystems and Society **72**(5), 577–592 (2023) [https://doi.org/10.2166/](https://doi.org/10.2166/aqua.2023.067)  
709 [aqua.2023.067](https://doi.org/10.2166/aqua.2023.067)
- 710 Beesley, L., Moreno-Jiménez, E., Gomez-Eyles, J.L.: Effects of biochar and green-  
711 waste compost amendments on mobility, bioavailability and toxicity of inorganic  
712 and organic contaminants in a multi-element polluted soil. Environmental Pollution  
713 **158**(6), 2282–2287 (2010) <https://doi.org/10.1016/j.envpol.2010.02.003>

- 714 Campion, L., Bekchanova, M., Malina, R., Kuppens, T.: The costs and benefits of  
715 biochar production and use: A systematic review. *Journal of Cleaner Production*  
716 **408**, 137138 (2023) <https://doi.org/10.1016/j.jclepro.2023.137138>
- 717 Cui, X., Wang, J., Wang, X., Du, G., Khan, K.Y., Yan, B., Cheng, Z., Chen, G.: Pyrol-  
718 ysis of exhausted hydrochar sorbent for cadmium separation and biochar regenera-  
719 tion. *Chemosphere* **306** (2022) <https://doi.org/10.1016/j.chemosphere.2022.135546>
- 720 Dentz, M., Lester, D.R., Speetjens, M.F.M.: Editorial to the special issue: Mixing in  
721 porous media. *Transport in Porous Media* **146**(1-2), 1–4 (2023) [https://doi.org/10.](https://doi.org/10.1007/s11242-022-01899-w)  
722 [1007/s11242-022-01899-w](https://doi.org/10.1007/s11242-022-01899-w)
- 723 Dawood, S., Sen, T.K., Phan, C.: Performance and dynamic modelling of biochar and  
724 kaolin packed bed adsorption column for aqueous phase methylene blue (mb) dye  
725 removal. *Environmental Technology* **40**(28), 3762–3772 (2019) [https://doi.org/10.](https://doi.org/10.1080/09593330.2018.1491065)  
726 [1080/09593330.2018.1491065](https://doi.org/10.1080/09593330.2018.1491065)
- 727 Gupta, S., Sireesha, S., Sreedhar, I., Patel, C.M., Anitha, K.L.: Latest trends in heavy  
728 metal removal from wastewater by biochar based sorbents. *Journal of Water Process*  
729 *Engineering* **38** (2020) <https://doi.org/10.1016/j.jwpe.2020.101561>
- 730 Guo, Z., Zheng, C., Shi, B.: Discrete lattice effects on the forcing term in the lattice  
731 boltzmann method. *Phys. Rev. E* **65** (2002) [https://doi.org/10.1103/PhysRevE.65.](https://doi.org/10.1103/PhysRevE.65.046308)  
732 [046308](https://doi.org/10.1103/PhysRevE.65.046308)
- 733 Huang, J., Hu, Z., Yong, W.-A.: Second-order curved boundary treatments of the  
734 lattice boltzmann method for convection–diffusion equations. *Journal of Computa-*  
735 *tional Physics* **310**, 26–44 (2016) <https://doi.org/10.1016/j.jcp.2016.01.008>
- 736 Huang, J., Yong, W.-A.: Boundary conditions of the lattice boltzmann method for  
737 convection–diffusion equations. *Journal of Computational Physics* **300**, 70–91 (2015)

- 738 <https://doi.org/10.1016/j.jcp.2015.07.045>
- 739 Jareteg, A., Maggiolo, D., Sasic, S., Ström, H.: On the roles of interstitial liquid  
740 and particle shape in modulating microstructural effects in packed-bed adsorbers.  
741 Chemical Engineering Research and Design **177**, 682–693 (2022) [https://doi.org/](https://doi.org/10.1016/j.cherd.2021.11.031)  
742 [10.1016/j.cherd.2021.11.031](https://doi.org/10.1016/j.cherd.2021.11.031)
- 743 Ji, G., Xing, Y., You, T.: Biochar as adsorbents for environmental microplastics and  
744 nanoplastics removal. Journal of Environmental Chemical Engineering **12**(5) (2024)  
745 <https://doi.org/10.1016/j.jece.2024.113377>
- 746 Khan, N., Chowdhary, P., Gnansounou, E., Chaturvedi, P.: Biochar and environmen-  
747 tal sustainability: Emerging trends and techno-economic perspectives. Bioresource  
748 Technology **332**, 125102 (2021) <https://doi.org/10.1016/j.biortech.2021.125102>
- 749 Kuoppamäki, K., Hagner, M., Lehvävirta, S., Setälä, H.: Biochar amendment in the  
750 green roof substrate affects runoff quality and quantity. Ecological Engineering **88**,  
751 1–9 (2016) <https://doi.org/10.1016/j.ecoleng.2015.12.010>
- 752 Lee, J., Kwon, E.E.: Biochar in green roofs. Journal of Building Engineering **89** (2024)  
753 <https://doi.org/10.1016/j.jobe.2024.109272>
- 754 Liapis, A.I., Meyers, J.J., Crosser, O.K.: Modeling and simulation of the dynamic  
755 behavior of monoliths: Effects of pore structure from pore network model analysis  
756 and comparison with columns packed with porous spherical particles. Journal of  
757 Chromatography A **865**(1-2), 13–25 (1999) [https://doi.org/10.1016/S0021-9673\(99\)](https://doi.org/10.1016/S0021-9673(99)01031-6)  
758 [01031-6](https://doi.org/10.1016/S0021-9673(99)01031-6)
- 759 Li, Z.-Z., Min, T., Kang, Q., He, Y.-L., Tao, W.-Q.: Investigation of methane adsorp-  
760 tion and its effect on gas transport in shale matrix through microscale and mesoscale  
761 simulations. International Journal of Heat and Mass Transfer **98**, 675–686 (2016)

- 762 <https://doi.org/10.1016/j.ijheatmasstransfer.2016.03.039>
- 763 Marin, P., Borba, C.E., Módenes, A.N., Espinoza-Quñones, F.R., De Oliveira, S.P.D.,  
 764 Kroumov, A.D.: Determination of the mass transfer limiting step of dye adsorption  
 765 onto commercial adsorbent by using mathematical models. *Environmental Technol-*  
 766 *ogy* **35**(18), 2356–2364 (2014) <https://doi.org/10.1080/09593330.2014.904445>
- 767 Maggiolo, D., Modin, O., Kalagasidis, A.S.: Transition from diffusion to advec-  
 768 tion controlled contaminant adsorption in saturated chemically heterogeneous  
 769 porous subsurfaces. *Phys. Rev. Fluids* **8**, 024502 (2023) [https://doi.org/10.1103/](https://doi.org/10.1103/PhysRevFluids.8.024502)  
 770 [PhysRevFluids.8.024502](https://doi.org/10.1103/PhysRevFluids.8.024502)
- 771 Mitra, S., Muttakin, M., Thu, K., Saha, B.B.: Study on the influence of adsorbent  
 772 particle size and heat exchanger aspect ratio on dynamic adsorption characteris-  
 773 tics. *Applied Thermal Engineering* **133**, 764–773 (2018) [https://doi.org/10.1016/j.](https://doi.org/10.1016/j.applthermaleng.2018.01.015)  
 774 [applthermaleng.2018.01.015](https://doi.org/10.1016/j.applthermaleng.2018.01.015)
- 775 Novotný, M., Marković, M., Raček, J., Šipka, M., Chorazy, T., Tošić, I., Hlavínek,  
 776 P.: The use of biochar made from biomass and biosolids as a substrate for green  
 777 infrastructure: A review. *Sustainable Chemistry and Pharmacy* **32** (2023) [https:](https://doi.org/10.1016/j.scp.2023.100999)  
 778 [//doi.org/10.1016/j.scp.2023.100999](https://doi.org/10.1016/j.scp.2023.100999)
- 779 Premarathna, K.S.D., Biswas, J.K., Kumar, M., Varjani, S., Mikan, B., Show, P.L.,  
 780 Lau, S.Y., Novo, L.A.B., Vithanage, M.: Biofilters and bioretention systems: the  
 781 role of biochar in the blue-green city concept for stormwater management. *Envi-*  
 782 *ronmental Science: Water Research and Technology* **9**(12), 3103–3119 (2023) [https:](https://doi.org/10.1039/d3ew00054k)  
 783 [//doi.org/10.1039/d3ew00054k](https://doi.org/10.1039/d3ew00054k)
- 784 Pita, M., Fernández-Andrade, K.J., Quiroz-Fernández, S., Rodríguez-Díaz, J.M., Díaz,

- 785 C.A.: Assessment of biomass as an effective adsorbent for the removal of pharmaceu-  
 786 tical compounds: A literature review. *Case Studies in Chemical and Environmental*  
 787 *Engineering* **9**, 100596 (2024) <https://doi.org/10.1016/j.cscee.2023.100596>
- 788 Pröll, T., Schöny, G., Sprachmann, G., Hofbauer, H.: Introduction and evaluation of  
 789 a double loop staged fluidized bed system for post-combustion co<sub>2</sub> capture using  
 790 solid sorbents in a continuous temperature swing adsorption process. *Chemical*  
 791 *Engineering Science* **141**, 166–174 (2016) <https://doi.org/10.1016/j.ces.2015.11.005>
- 792 Robin, D., Arnaud, C., Philippe, S.: Model of reactive transport within a light pho-  
 793 tocatalytic textile. *International Journal of Chemical Reactor Engineering* **14**(1),  
 794 269–281 (2016) <https://doi.org/10.1515/ijcre-2015-0060>
- 795 Rajabi, H., Hadi Mosleh, M., Prakoso, T., Ghaemi, N., Mandal, P., Lea-Langton, A.,  
 796 Sedighi, M.: Competitive adsorption of multicomponent volatile organic compounds  
 797 on biochar. *Chemosphere* **283** (2021) [https://doi.org/10.1016/j.chemosphere.2021.](https://doi.org/10.1016/j.chemosphere.2021.131288)  
 798 [131288](https://doi.org/10.1016/j.chemosphere.2021.131288)
- 799 Succi, S.: *The Lattice Boltzmann Equation: for Fluid Dynamics and Beyond*. Oxford  
 800 University Press, Oxford (2001)
- 801 Senadheera, S.S., Withana, P.A., Lim, J.Y., Ok, Y.S., Senadheera, S.S., Lim, J.Y.,  
 802 Rhee, J.H., Ok, Y.S., Lim, J.Y., Rhee, J.H., You, S., Chang, S.X., Wang, F.,  
 803 Wang, F.: Carbon negative biochar systems contribute to sustainable urban green  
 804 infrastructure: a critical review. *Green Chemistry* (2024) [https://doi.org/10.1039/](https://doi.org/10.1039/d4gc03071k)  
 805 [d4gc03071k](https://doi.org/10.1039/d4gc03071k)
- 806 Verma, N., Mewes, D.: Lattice boltzmann methods for simulation of micro and  
 807 macrotransport in a packed bed of porous adsorbents under non-isothermal con-  
 808 dition. *Computers & Mathematics with Applications* **58**(5), 1003–1014 (2009)

809 <https://doi.org/10.1016/j.camwa.2009.02.023>

810 World Meteorological Organization's World Weather & Climate Extremes Archive.  
 811 <https://wmo.asu.edu/content/world-greatest-sixty-minute-one-hour-rainfall>.  
 812 Accessed: 2024-01-28

813 Wang, H., Qin, J., Hu, Y.: Are green roofs a source or sink of runoff pollutants?  
 814 Ecological Engineering **107**, 65–70 (2017) [https://doi.org/10.1016/j.ecoleng.2017.](https://doi.org/10.1016/j.ecoleng.2017.06.035)  
 815 [06.035](https://doi.org/10.1016/j.ecoleng.2017.06.035)

816 Xiang, L., Liu, S., Ye, S., Yang, H., Song, B., Qin, F., Shen, M., Tan, C., Zeng,  
 817 G., Tan, X.: Potential hazards of biochar: The negative environmental impacts of  
 818 biochar applications. Journal of Hazardous Materials **420**, 126611 (2021) [https:](https://doi.org/10.1016/j.jhazmat.2021.126611)  
 819 [//doi.org/10.1016/j.jhazmat.2021.126611](https://doi.org/10.1016/j.jhazmat.2021.126611)

820 Ye, L., Camps-Arbestain, M., Shen, Q., Lehmann, J., Singh, B., Sabir, M.: Biochar  
 821 effects on crop yields with and without fertilizer: A meta-analysis of field studies  
 822 using separate controls. Soil Use and Management **36**(1), 2–18 (2020) [https://doi.](https://doi.org/10.1111/sum.12546)  
 823 [org/10.1111/sum.12546](https://doi.org/10.1111/sum.12546)

824 Zanin Lima, J., Monici Raimondi Nauerth, I., Ferreira da Silva, E., José Pejon, O.,  
 825 Guimarães Silvestre Rodrigues, V.: Competitive sorption and desorption of cad-  
 826 mium, lead, and zinc onto peat, compost, and biochar. Journal of Environmental  
 827 Management **344**, 118515 (2023) <https://doi.org/10.1016/j.jenvman.2023.118515>

828 Zakirov, T.R., Mikhailova, A.N., Varfolomeev, M.A., Yuan, C.: Pore-scale study of  
 829 dynamic adsorption of a water-soluble catalyst during drainage displacement in  
 830 porous media using lattice boltzmann simulations. International Communications in  
 831 Heat and Mass Transfer **145** (2023) [https://doi.org/10.1016/j.icheatmasstransfer.](https://doi.org/10.1016/j.icheatmasstransfer.2023.106810)  
 832 [2023.106810](https://doi.org/10.1016/j.icheatmasstransfer.2023.106810)

## 833 **Declarations**

- 834 • Funding: FORMAS Grant No. 2019–01261
- 835
- 836 • Competing Interests: The authors have no competing interests to declare that are  
837 relevant to the content of this article.
- 838
- 839 • Ethics approval and consent to participate: Not applicable
- 840
- 841 • Consent for publication: Not applicable
- 842
- 843 • Data availability: The datasets generated during and/or analysed during the cur-  
844 rent study are available from the corresponding author on reasonable request.
- 845
- 846 • Materials availability: Not applicable
- 847
- 848 • Code availability: Not applicable
- 849
- 850 • Author contribution: Conceptualization: Dario Maggiolo, Oskar Modin, Angela  
851 Sasic Kalagasidis; Formal Analysis: Kaj Pettersson, Albin Nordlander, Dario Mag-  
852 giolo; Funding acquisition: Dario Maggiolo; Investigation: Kaj Pettersson, Albin  
853 Nordlander; Methodology: Dario Maggiolo, Oskar Modin; Project administra-  
854 tion: Dario Maggiolo; Resources: Dario Maggiolo, Angela Sasic Kalagasidis, Oskar  
855 Modin; Software: Kaj Pettersson, Dario Maggiolo, Albin Nordlander; Supervi-  
856 sion: Dario Maggiolo, Oskar Modin; Validation: Kaj Pettersson, Albin Nordlander;  
857 Visualization: Kaj Pettersson, Albin Nordlander; Writing – original draft: Kaj Pet-  
858 tersson; Writing – review & editing: Kaj Pettersson, Dario Maggiolo, Angela Sasic  
859 Kalagasidis, Oskar Modin